# MonoDETR: Depth-guided Transformer for Monocular 3D Object Detection

Renrui Zhang $^{1,3}$ , Han Qiu $^1$ , Tai Wang $^{1,3}$ , Ziyu Guo $^2$ , Xuanzhuo Xu $^2$ , Yu Qiao $^1$ , Peng Gao $^{\dagger 1}$ , Hongsheng Li $^3$ 

<sup>1</sup>Shanghai AI Laboratory

<sup>2</sup> Peking University <sup>3</sup> The Chinese University of Hong Kong {zhangrenrui, qiuhan, gaopeng}@pjlab.org.cn

<sup>†</sup> Corresponding author

#### **Abstract**

Monocular 3D object detection has long been a challenging task in autonomous driving, which requires to decode 3D predictions solely from a single 2D image. Most existing methods follow conventional 2D object detectors to localize objects based on their centers, and predict 3D attributes by neighboring features around the centers. However, only using local features is insufficient to understand the scene-level 3D spatial structures and ignore the inter-object depth relations from contextual cues. In this paper, we introduce a novel framework for **Mono**cular **D**Etection with a depth-guided **TR**ansformer, named **MonoDETR**. The vanilla transformer is modified to be depth-aware and the whole detection process is then guided by depth. Specifically, we represent 3D object candidates as a set of queries and adopt an attention-based depth encoder to produce non-local depth embeddings of the input image. Then, we propose a depth-guided decoder with depth cross-attention modules to conduct both inter-query and query-scene depth feature interactions. In this way, each object query estimates its 3D attributes adaptively from the depth-guided regions from the image and is no longer constrained to use only neighboring visual features. MonoDETR is an end-to-end network without extra data or NMS post-processing and achieves state-of-the-art performance on KITTI benchmark with significant gains. Extensive ablation studies demonstrate the effectiveness of our approach and its potential to serve as a transformer baseline for future monocular 3D object detection research. Code is available at https://github.com/ZrrSkywalker/MonoDETR.

# 1 Introduction

It is an important capability for autonomous driving vehicles and robots to understand the scene and objects in the 3D space. With a wide range of applications, 3D object detection is more challenging than its 2D counterparts due to the complex real-world spatial circumstances. Compared to methods based on LiDAR-scanned point clouds [51, 18, 33] and binocular images [13, 15], 3D object detection from monocular images [8, 2, 26] is the most difficult, which generally does not rely on environment depth measurements. The detection accuracy thus severely suffers from the ill-posed depth estimation, leading to inferior performance.

Existing monocular 3D detection methods [41, 26, 46, 47, 24] mostly follow the pipelines of traditional 2D object detectors [31, 21, 38, 50] to first localize objects in the image by detecting their 2D or projected 3D centers from heatmaps. Then, the visual features around each object center are aggregated to predict the object's 3D properties, e.g., depth, 3D sizes, and orientation. Such center-guided methods are illustrated in Figure 1 (Top). Although it is conceptually straightforward,

Preprint. Under review.

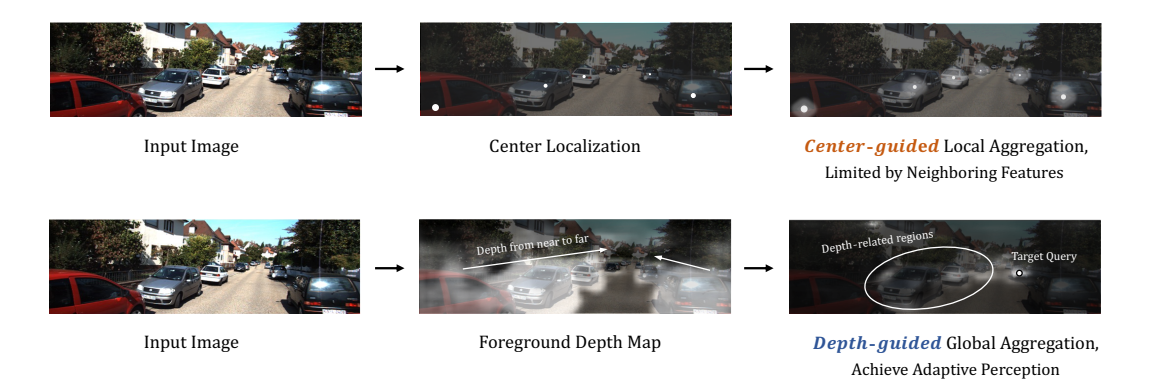


Figure 1: Center-guided Methods (Top) and our Depth-guided Paradigms (Bottom). Existing center-guided methods utilize features around the centers to predict 3D attributes of objects, while ours guides the whole process by a predicted foreground depth map and adaptively aggregates depth features from the entire scene. The lower right picture denotes the attention map in the depth cross-attention layer.

merely using local features around the predicted object centers is insufficient to understand the scene-level geometric cues for accurately estimating the depth of objects.

To tackle this issue, we propose a transformer-based framework, MonoDETR. It presents a novel depth-guided feature aggregation scheme to adaptively estimate each object's 3D attributes based on global context, as shown in Figure 1 (Bottom). We modify the transformer of our MonoDETR to be depth-aware, which consists of a visual encoder, a depth encoder, and a depth-guided decoder to better capture scene-level depth cues via attention mechanisms. Specifically, for an input image, we first utilize a feature backbone along with a lightweight depth predictor to encode its visual and depth features. To endow effective depth signals into the depth features, we generate a foreground depth map on top and supervise it only by object-wise depth labels. Then, we specialize two concurrent encoders to generate the global depth and visual embeddings via self-attention layers, which respectively capture the long-range spatial and appearance information of the input image. On top of that, we utilize a depth-guided decoder to aggregate informative features from the two embeddings and detect 3D objects with a set of learnable queries. Each decoder block contains a depth cross-attention layer, an inter-query self-attention layer, and a visual cross-attention layer in order. The foremost depth cross-attention layer enables each query to adaptively capture geometric cues from the depth-related regions on the image, and model inter-object depth relations based on global context. Then, the following two attention modules further allow object queries to interact features with each other and collect semantic information from the scene-level visual appearances. By such depth-guided decoding, the 3D-attribute prediction of each object query, especially the depth, can be largely boosted, and is no longer constrained by the limited visual features around centers.

To our best knowledge, MonoDETR is the first end-to-end DETR-based network for monocular 3D object detection without non-maximum suppression (NMS), pre-defined anchors, or IoU-based label assignment. MonoDETR requires no extra input data, such as multi-view images, dense depth maps or LiDAR, and only supervises the depth features by the already provided object-wise depth labels. In addition, different from recent center-guided methods with sophisticated geometric priors [47, 46, 24], MonoDETR adopts minimal 3D inductive bias and still achieves *state-of-the-art* performance.

We summarize the contributions of our paper as follows:

- 1. We propose MonoDETR, the first end-to-end DETR-based network for monocular 3D object detection without extra inputs or NMS, which adopts a depth-guided scheme for aggregating features from the depth-related regions in global context.
- 2. The depth-guided transformer of MonoDETR enables object queries to adaptively collect informative spatial and appearance information of the scene, and better model the inter-object relations to assist the depth estimation.

 MonoDETR introduces marginal handcrafted designs or geometric priors, and achieves stateof-the-art performance on KITTI test and val sets, outperforming all existing center-guided methods with significant gains.

#### 2 Related Work

Monocular 3D Object Detection without Extra Data. Except for methods assisted by additional inputs, such as depth maps [25, 11, 40], multiple views [43], CAD models [23], and LiDAR [6, 30, 17], standard monocular detectors take as input only a single image and mostly adopt center-guided pipelines following conventional 2D detectors [31, 21, 38, 50]. Deep3DBox [29] firstly introduces discretized representation with 2D-3D prospective constraints to predict accurate object poses. M3D-RPN [2] designs a depth-aware convolution along with 3D anchors to generate better 3D region proposals. With very few handcrafted modules, SMOKE [22] and FCOS3D [41] propose concise architectures for one-stage monocular detection built on CenterNet [50] and FCOS [38], respectively. MonoDLE [26] and PGD [42] analyze depth errors on top and enhance their performance with customized designs. To further strengthen the detection accuracy, recent methods have introduced more effective but complicated geometric priors into the networks. MonoPair [9] considers adjacent object pairs and parses their spatial relations with uncertainty. RTM3D [19] predicts 2D-3D keypoints of objects and optimizes the bounding box by nonlinear least squares. MonoFlex [46] conducts uncertainty-guided depth ensemble and categorizes different objects for distinctive processing. GUP-Net [24] solves the error amplification problem by geometry-guided depth uncertainty and collocates a hierarchical learning strategy to reduce the training instability. Although the above geometricdependent designs largely promote the performance, the center-guided pipelines are still limited by the local features around centers. In contrast, our proposed MonoDETR adopts a depth-guided feature aggregation scheme via a depth-guided transformer and discards the dependency for center detection. MonoDETR leverages attention mechanisms to adaptively explore depth cues from depth-related regions in global context and achieves leading performance with minimal 3D-specific inductive biases.

**Object Detection with Transformers.** 2D object detectors [20, 21, 38] have achieved excellent performance in recent years but have cumbersome post-processing such as non-maximum suppression (NMS) [31, 1]. To circumvent it, the seminal work DETR [4] constructs a novel framework by adapting the powerful transformer [39] in natural language processing into computer vision for 2D detection. DETR detects objects on the image by an encoder-decoder paradigm and outputs set prediction aided by Hungary Matching Algorithm [4]. However, due to the quadratic computational complexity of attention, DETR requires the expensive 500 epochs to be fully trained. To accelerate the convergence, Deformable DETR [52] designs the sparse deformable attention mechanism and achieves better performance with only 50-epoch training. ACT [48] boosts the efficiency for both time and memory by introducing adaptive clustering algorithms during inference. SMCA [12] proposes the Gaussian-modulated co-attention mechanism, which refocuses the attention of each query into object-centric areas. Besides, DETR is further enhanced by placing anchors [44], redesigning as two stages [36, 37], setting conditional attention [27], embedding dense priors [45] and so on [10, 28]. Our MonoDETR first introduces DETR to conduct monocular 3D object detection, which inherits its superiority for non-local encoding and is also free from the NMS post-processing. Based on its visual encoder and decoder, we newly equip a depth encoder and a depth-guided decoder for adaptive scene-level depth understanding, which significantly improves the accuracy for monocular 3D object detection.

### 3 Method

The overall framework of MonoDETR is shown in Figure 2, which consists of: a feature backbone, a depth predictor, a depth-guided transformer with a set of object queries, and several detection heads. In Section 3.1, we first introduce the feature extraction of the input image and the foreground depth map. Then in Section 3.2, we detail our depth-guided transformer to adaptively aggregate features for the queries. Finally in Section 3.3, we present our prediction of 3D attributes and the loss functions.

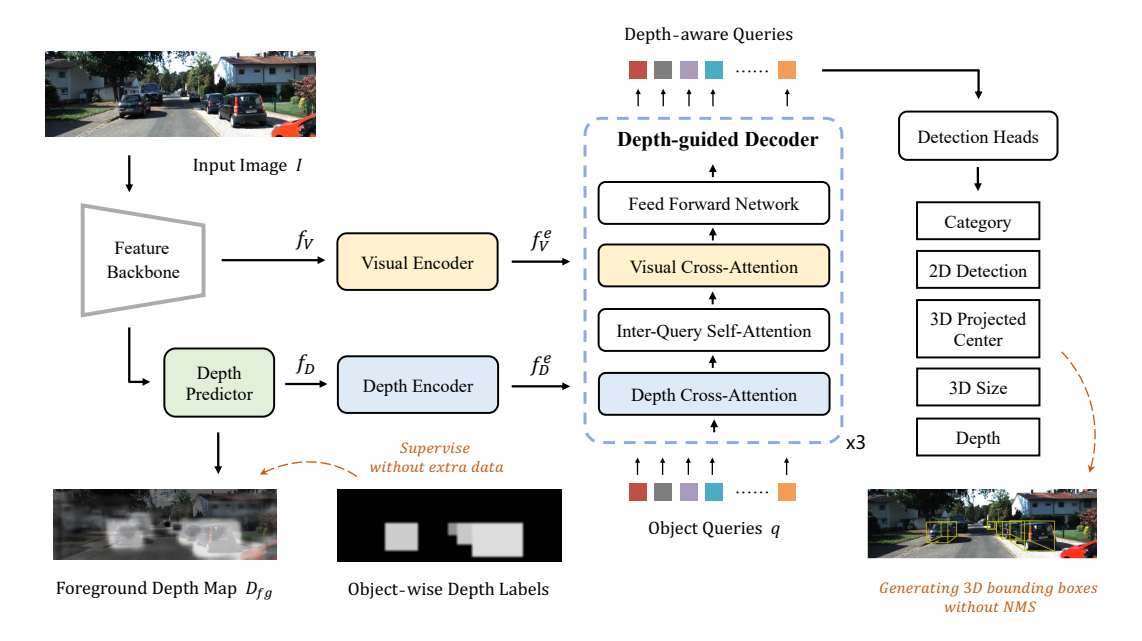


Figure 2: **Overall pipeline of MonoDETR.** We acquire the visual and depth features of the input image and utilize two parallel encoders for non-local encoding. Then, we propose a depth-guided decoder to adaptively aggregate scene-level features for object queries in global context.

#### 3.1 Features Extraction

Taking as input a raw image, our framework utilizes a feature backbone, e.g., ResNet-50 [16], and a lightweight depth predictor to generate both visual and depth features of the input image.

**Visual Features.** Given the image  $I \in \mathbb{R}^{H \times W \times 3}$ , where H and W denote its height and width, we obtain its multi-scale feature maps,  $f_{\frac{1}{8}}$ ,  $f_{\frac{1}{16}}$ , and  $f_{\frac{1}{32}}$ , from the last three stages of ResNet-50. Their downsample ratios are  $\frac{1}{8}$ ,  $\frac{1}{16}$  and  $\frac{1}{32}$ , respectively. We regard the highest-level  $f_{\frac{1}{32}} \in \mathbb{R}^{\frac{H}{32} \times \frac{W}{32} \times C}$  as visual features  $f_V$  of the input image.

**Depth Features.** We obtain the depth features from the image by a lightweight depth predictor, as shown in Figure 3 (Left). We first unify the sizes of three-level features to the same  $\frac{1}{16}$  downsample ratio via nearest-neighbor sampling, and fuse them by element-wise addition. By this, we integrate multi-scale semantics and also preserve the fine-grained information of the image. Then, we apply two  $3\times 3$  convolutions to obtain the depth features  $f_D\in\mathbb{R}^{\frac{H}{16}\times\frac{W}{16}\times C}$  for the input image. To enforce  $f_D$  to encode informative depth information, we predict a foreground depth map  $D_{fg}$  on top of  $f_D$  and supervise it only by object-wise depth labels, without extra dense depth annotations. The pixels within the same 2D box of an object are assigned with the same depth label of the object. For pixels within multiple boxes simultaneously, we select the depth label of the object that is nearest to the camera, which accords with the visual appearance of the image.

Foreground Depth Map. To supervise the depth features, we apply a  $1 \times 1$  convolution on top of  $f_D$  to predict the foreground depth map  $D_{fg} \in \mathbb{R}^{\frac{H}{16} \times \frac{W}{16} \times (k+1)}$ . Here, we discretize the depth into k+1 bins following [30], where the first ordinal k bins represent foreground depth and the last one denotes the background. We adopt linear-increasing discretization (LID), since the depth estimation of farther objects inherently yields larger errors and can be suppressed with a wider categorization interval. We limit the foreground depth values within  $[d_{min}, d_{max}]$  and set both the first interval length and the common difference of LID as  $\delta$ . We then categorize a ground-truth depth label d of an object into the k-th bin as

$$k = \lfloor -0.5 + 0.5\sqrt{1 + \frac{8(d - d_{min})}{\delta}} \rfloor$$
, where  $\delta = \frac{2(d_{max} - d_{min})}{k(k+1)}$ . (1)

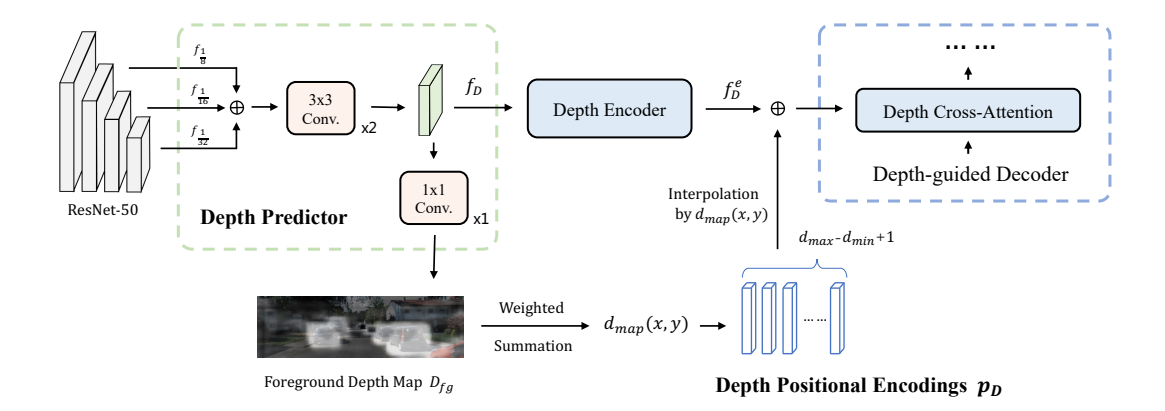


Figure 3: **Details of depth predictor (Left) and depth positional encodings (Right).** We utilize the depth predictor to output the depth features and foreground depth map of the input image. In the depth cross-attention layer, we adopt learnbale positional encodings for the depth embeddings by depth interpolation.

For pixels within background area, we directly assign them to the (k+1)-th category. We use Focal loss [21] to supervise the categorical depth prediction for each pixel in  $D_{fg}$ , denoted as  $\mathcal{L}_{dmap}$ .

#### 3.2 Depth-guided Transformer

The transformer of MonoDETR is composed of a visual encoder, a depth encoder and a depth-guided decoder. The two encoders produce non-local visual and depth embeddings, and the depth-guided decoder enables object queries to adaptively aggregate scene-level features in global context.

Visual and Depth Encoders. Given depth and visual features  $f_D, f_V$ , we specialize two encoders to independently produce their scene-level embeddings with global receptive fields, denoted as  $f_D^e, f_V^e$ . We set three blocks for the visual encoder and one block for depth encoder. Each encoder block consists of a self-attention layer and a feed-forward neural network (FFN). By the global self-attention, the depth encoder explores long-range dependencies of depth values from different foreground areas, which provides the network with non-local cues of the entire stereo space. In addition, the decoupling of depth and visual encoders allows them to better learn features for themselves, respectively encoding the appearance and spatial information of the input image.

**Depth-guided Decoder.** Based on the non-local visual and depth embeddings  $f_D^e$ ,  $f_V^e$ , we utilize a set of learnable object queries  $q \in \mathbb{R}^{N \times C}$  to detect 3D objects via the depth-guided decoder, where N denotes the pre-defined maximum number of objects in the input image. Each decoder block sequentially consists of a depth cross-attention layer, an inter-query self-attention layer, a visual cross-attention layer and an FFN. Specifically, the queries first aggregate informative depth features from  $f_D^e$  via the depth cross-attention layer, in which we linearly transform the object queries and depth embeddings into queries, keys and values,

$$Q_q = \operatorname{Linear}(q), \quad K_D, V_D = \operatorname{Linear}(f_D^e),$$
 (2)

where  $Q_q \in \mathbb{R}^{N \times C}$  and  $K_D, V_D \in \mathbb{R}^{\frac{HW}{16^2} \times C}$ . Then, we calculate the query-depth attention map  $A_D \in \mathbb{R}^{N \times \frac{HW}{16^2}}$ , and aggregate related depth features weighted by  $A_D$  to produce the depth-aware queries q', formulated as,

$$A_D = \operatorname{Softmax}(Q_q K_D^T / \sqrt{C}), \quad q' = \operatorname{Linear}(A_D V_D).$$
 (3)

Such a depth cross-attention layer enables each object query to adaptively explore spatial cues from depth-related regions of the image. Thus, the query can better understand the scene-level spatial structures and model inter-object geometric relations to assist the depth estimation. Then, the queries pass through the inter-query self-attention layer for further feature interactions between queries, which avoids predicting duplicate boxes for the same object. Finally via the visual cross-attention

layer, the queries collect appearance features from  $f_V^e$  to acquire semantic information of the image. We stack three decoder blocks for fusing scene-level depth cues and visual appearances into object queries, which fully achieves the depth-guided feature aggregation scheme.

**Depth Positional Encodings.** In the depth cross-attention layer, we propose learnable depth positional encodings for  $f_D^e$  instead of using sinusoidal functions as other attention modules. As shown in Figure 3 (Right), we maintain a set of learnable embeddings,  $p_D \in \mathbb{R}^{(d_{max}-d_{min}+1)\times C}$ , where each row encodes the depth positional information for a meter, ranging from  $d_{min}$  to  $d_{max}$ . For each pixel (x,y) in  $f_D^e$ , we first obtain the (k+1)-categorical depth prediction confidence,  $D_{fg}(x,y) \in \mathbb{R}^{k+1}$ , from  $D_{fg}$ , each channel of which denotes the predicted confidence for the corresponding depth bin. The estimated depth of pixel (x,y) can then be obtain by the weighted summation of the depth-bin confidences and their corresponding depths, which is denoted as  $d_{map}(x,y)$ . Then, we linearly interpolate  $p_D$  according to the depth  $d_{map}(x,y)$  to obtain the depth positional encoding for the pixel (x,y). By pixel-wisely adding  $f_D^e$  with such encodings, object queries can capture more sufficient depth cues in the depth cross-attention layer and better understand the scene's 3D structures.

#### 3.3 Detection Heads and Loss

After the depth-guided transformer, the depth-aware object queries are fed into a series of MLP-based heads for 3D-attribute estimation. During inference, we integrate the attributes to recover 3D bounding boxes directly as outputs, requiring no NMS post-processing. For training, we respectively compute the loss for each query, and utilize Hungarian algorithm [5] to match the orderless queries with ground-truth object labels, without any rule-based label assignment.

Attributes Prediction. By the detection heads, we predict six attributes for each query: object category, 2D size (l,r,t,b), projected 3D center  $(x_{3D},y_{3D})$ , depth  $d_{reg}$ , 3D size  $(h_{3D},w_{3D},l_{3D})$  and orientation  $\alpha$ . Therein, (l,r,t,b) denote the distances from four sides of the 2D bounding box to the projected 3D center  $(x_{3D},y_{3D})$ , and both the (l,r,t,b) and  $(x_{3D},y_{3D})$  are normalized from 0 to 1 by the image size. To estimate the final object depth  $d_{pred}$  more accurately, we average three predicted values:  $d_{reg}$  regressed by the detection head,  $d_{geo}$  converted by the predicted 2D and 3D sizes, and  $d_{map}(x_{3D},y_{3D})$  interpolated from  $D_{fg}$ . We formulate as,

$$d_{geo} = f \frac{h_{3D}}{t+b}, \quad d_{pred} = (d_{reg} + d_{geo} + d_{map}(x_{3D}, y_{3D}))/3, \tag{4}$$

where  $h_{3D}$  and t + b denote the predicted heights of 3D and 2D sizes, and f denotes the camera focal length. More details for the attributes and loss functions are listed in Appendix.

**Bipartite Matching.** To correctly match each query with a ground-truth object, we calculate the loss for each query-label pair and utilize Hungarian algorithm to find the globally optimal matching. For each pair, we integrate the losses of six attributes into two groups. The first group contains object category, 2D size and the projected 3D center, since these attributes mainly concern 2D visual appearances of the image. The second group consists of the depth, 3D size and orientation, which are 3D spatial properties of the object. We respectively sum the losses of two groups and denote them as  $\mathcal{L}_{2D}$  and  $\mathcal{L}_{3D}$ . As the network generally predicts less accurate 3D attributes than 2D attributes, especially at the beginning of training, the value of  $\mathcal{L}_{3D}$  is unstable and would disturb the matching process. We only utilize  $\mathcal{L}_{2D}$  as the matching cost for matching each query-label pair.

**Overall Loss.** After query-label matching, we obtain  $N_{gt}$  valid pairs out of N queries, where  $N_{gt}$  denotes the number of ground-truth objects. Then, the overall loss of a training image is formulated as

$$\mathcal{L}_{overall} = \frac{1}{N_{gt}} \cdot \sum_{n=1}^{N_{gt}} (\mathcal{L}_{2D} + \mathcal{L}_{3D}) + \mathcal{L}_{dmap}, \tag{5}$$

where  $\mathcal{L}_{dmap}$  represents the loss of the predicted categorical foreground depth map  $D_{fg}$  as discussed in Section 3.1.

Table 1: **Performance of the car category on KITTI** *test* **and** *val* **sets.** We utilize bold numbers to highlight the best results, and color the second-best ones and our performance gain over them in blue.

Method	Extra data	T	est, $AP_3$	D	Те	st, $AP_{BI}$	$\Xi V$	1	Val, $AP_3$	D
Memod	Extra data	Easy	Mod.	Hard	Easy	Mod.	Hard	Easy	Mod.	Hard
PatchNet [25]		15.68	11.12	10.17	22.97	16.86	14.97	-	-	-
D4LCN [11]	Depth	16.65	11.72	9.51	22.51	16.02	12.55	-	-	-
DDMP-3D [40]		19.71	12.78	9.80	28.08	17.89	13.44	-	-	-
Kinematic3D [3]	Multi-frames	19.07	12.72	9.17	26.69	17.52	13.10	19.76	14.10	10.47
MonoRUn [6]		19.65	12.30	10.58	27.94	17.34	15.24	20.02	14.65	12.61
CaDDN [30]	LiDAR	19.17	13.41	11.46	27.94	18.91	17.19	23.57	16.31	13.84
MonoDTR [17]		21.99	15.39	12.73	28.59	20.38	17.14	24.52	18.57	15.51
AutoShape [23]	CAD	22.47	14.17	11.36	30.66	20.08	15.59	20.09	14.65	12.07
SMOKE [22]		14.03	9.76	7.84	20.83	14.49	12.75	14.76	12.85	11.50
MonoPair [9]		13.04	9.99	8.65	19.28	14.83	12.89	16.28	12.30	10.42
RTM3D [19]		13.61	10.09	8.18	-	-	-	19.47	16.29	15.57
PGD [42]		19.05	11.76	9.39	26.89	16.51	13.49	19.27	13.23	10.65
IAFA [49]	None	17.81	12.01	10.61	25.88	17.88	15.35	18.95	14.96	14.84
MonoDLE [26]	rtone	17.23	12.26	10.29	24.79	18.89	16.00	17.45	13.66	11.68
MonoRCNN [34]		18.36	12.65	10.03	25.48	18.11	14.10	16.61	13.19	10.65
MonoGeo [47]		18.85	13.81	11.52	25.86	18.99	16.19	18.45	14.48	12.87
MonoFlex [46]		19.94	13.89	12.07	28.23	19.75	16.89	23.64	17.51	14.83
GUPNet [24]		20.11	14.20	11.77	-	-	-	22.76	16.46	13.72
MonoDETR (Ours)	None	25.00	16.47	13.58	33.60	22.11	18.60	28.84	20.61	16.38
Improvement	v.s. second-best	+2.53	+1.08	+0.85	+2.94	+1.73	+1.41	+4.32	+2.04	+0.81

# 4 Experiments

### 4.1 Settings

**Dataset.** We test MonoDETR on the widely-adopted KITTI 3D object detection benchmark [14], including 7,481 training and 7,518 test images. We follow [7, 8] to split the training images into 3,712 sub-training set and 3,769 val set. We report the detection results with three-level difficulties, easy, moderate and hard, and evaluate the performance with the average precision (AP) of bounding boxes in 3D space and the bird-eye view, denoted as  $AP_{3D}$  and  $AP_{BEV}$ , respectively, which are at 40 recall positions. We report scores for the car category under the intersection-over-union (IoU) threshold of 0.7. The pedestrian and cyclist categories are in Appendix.

Implementation Details. We adopt ResNet-50 [16] as our feature backbone. To save GPU memory, we apply deformable attention mechanisms [52] for the visual encoder and visual cross-attention layers, and adopt the vanilla attention [5] to better capture global spatial structures for the depth encoder and depth cross-attention layers. We utilize 8 heads for all attention modules and set the number of queries N as 50. We set the channel C and the latent feature dimension of FFN and MLP-based detection heads both as 256. For the foreground depth map, we set  $[d_{min}, d_{max}]$  as [0m, 60m] and the number of bins k as 80. On a single GeForce RTX 3090 GPU, we train MonoDETR for 195 epochs with batch size 16 and the learning rate  $2 \times 10^{-4}$ . We adopt AdamW optimizer with weight decay  $10^{-4}$  and decrease the learning rate at 125 and 165 epochs by a factor of 0.1.

#### 4.2 Performance Comparison

As shown in Table 1, with the proposed depth-guided transformer, MonoDETR achieves state-of-the-art performance for the car category on official KIITI test set. MonoDETR exceeds all existing methods including those with different additional inputs and surpasses the second-best under easy, moderate and hard levels respectively by +2.53%, +1.08% and +0.85% in terms of  $AP_{3D}$ , and by +2.94%, +1.73% and +1.41% in terms of  $AP_{BEV}$ . For the KITTI val set, MonoDETR also achieves the best performance, surpassing the second-best by +5.20%, +3.10% and +0.81% in  $AP_{3D}$ . Therein, the powerful MonoDTR [17] also applies transformers to fuse the depth features to benefit the detection, but it is still a center-guided method without object queries for adaptive feature aggregation, and highly relies on additional depth supervision, anchors and NMS post-processing. In contrast, our MonoDETR requires no extra inputs or NMS, and contains marginal geometric priors, showing its simplicity and effectiveness for monocular 3D object detection.

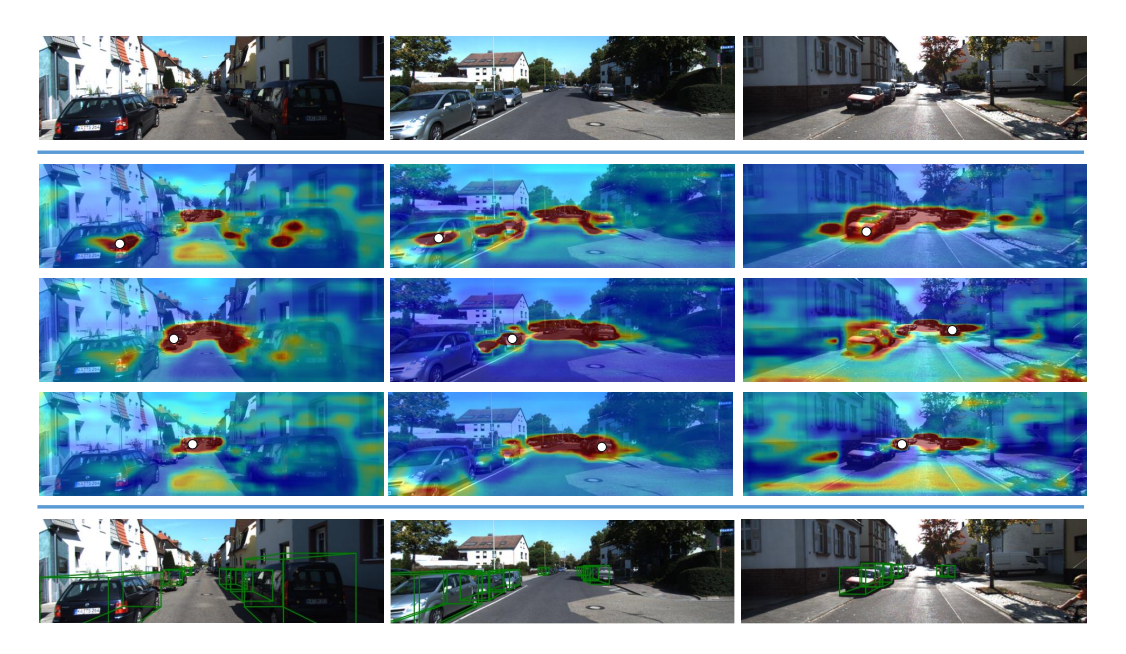


Figure 4: Visualizations of attention maps  $A_D$  in the depth cross-attention layer. The top and bottom rows represent the input images and detection results. The middle three rows are the attention maps of the target queries (denoted as white dots). Hotter colors indicate higher attention weights.

Table 2:**Effectiveness of depth-guided transformer.** 'Depth-guided Trans.', 'Depth CA' and 'Depth Pos.' denote the depth-guided transformer, depth cross-attention layer and depth positional encodings.

Table 3: The design of depth encoder. 'Deform. SA' and 'Global  $SA_{\times 2}$ ' denote one-block deformable self-attention and two-block vanilla self-attention.

Architecture	Easy	Mod.	Hard	-	Mechanism	Easy	Mod.	Hard
MonoDETR	28.84	20.61	16.38		Global SA	28.84	20.61	16.38
w/o Depth-guided Trans.	19.69	15.15	13.93		Deform. SA	26.43	18.91	15.55
w/o Depth Encoder	24.25	18.38	15.41		Global $SA_{\times 2}$	26.57	19.44	16.02
w/o Separate Depth CA	24.94	18.41	15.39		$3\times3$ Conv. $\times2$	25.55	18.36	15.28
w/o Depth Pos. $p_D$	24.04	18.11	15.10		FFN	25.65	18.52	15.34

#### 4.3 Ablation Studies

We report the  $AP_{3D}$  results of the car category on the KITTI val set for all ablation studies, which are conducted by modifying individual components of our final solution.

**Depth-guided Transformer.** We validate the effectiveness of our proposed depth-guided transformer by removing one of its components at a time. We first construct a center-guided variant of our approach by removing the entire transformer including the encoders and depth-guided decoder. We predict a 2D heatmap for object center detection and utilize local features to estimate the 3D attributes of objects (denoted as 'w/o Depth-guided Trans.' in Table 2). The absence of depth guidance greatly hurts the performance due to its limited receptive fields and non-adaptive feature aggregation. We then remove either the depth encoder, depth cross-attention layer, or the learnable depth positional encodings from our depth-guided transformer to validate their necessity. For 'w/o Depth Encoder', we directly feed the depth features  $f_D$  into the depth-guided decoder without non-local encoding. For 'w/o separate Depth CA', we fuse the depth and visual embeddings  $f_D^e$ ,  $f_V^e$  by element-wise addition, and apply only one cross-attention layer in each decoder block for the queries to aggregate the depth and visual features. As reported in the table, the above variants all lead to performance drops, demonstrating the effectiveness of individual modules in our depth-guided transformer.

'D', 'I', 'V' denote the depth cross-attention, interquery self-attention and visual cross-attention layers. 'Deform. Depth CA' represents deformable attention in the depth cross-attention layer.

Table 4: The design of depth-guided decoder. Table 5: Depth positional encodings. 'Meterwise  $p_D$ ' and 'k-bin  $p_D$ ' assigns learnable embeddings by meters and depth bins, respectively. 'sin/cos' denotes sinusoidal functions for positional encodings.

Architecture	Easy	Mod.	Hard
$D \to I \! \to V$	28.84	20.61	16.38
$I \to D {\to} V$	26.24	19.28	16.03
$I \to V {\to} D$	25.84	18.85	15.72
Deform. Depth CA	24.16	18.45	15.32

Settings	Easy	Mod.	Hard
Meter-wise $p_D$	28.84	20.61	16.38
$k$ -bin $p_D$ Depth sin/cos	24.58 26.05	18.33 19.18	15.23 15.97
2D sin/cos	24.65	18.11	15.16

**Depth Encoder.** The depth encoder produces non-local depth embeddings  $p_D^e$ , which are essential for queries to explore scene-level depth cues in the depth cross-attention layer. We experiment with different encoder designs in Table 3. 'Global  $SA(\times 2)$ ' denotes one or two blocks of vanilla self-attention layer with a global receptive field. 'Deform. SA' and '3×3 Conv.x2' represent oneblock of deformable attention [52] and three  $3 \times 3$  convolutions, respectively. As reported, a global understanding of the scene-level depth by self-attention layer performs the best.

**Depth-guided Decoder.** As the core component of our depth-guided paradigm, we explore how to better guide object queries q to aggregate depth features from  $f_D^e$  in Table 4. With the sequential inter-query self-attention and visual cross-attention layers, we experiment with three positions to integrate the depth cross-attention layer into each decoder block. We denote the three attention modules respectively as 'I', 'V' and 'D' in the table and the 'D  $\rightarrow$  I  $\rightarrow$  V' order achieves the highest performance. By placing 'D' in the front, each object query could first aggregate depth information to guide the remaining operations in each decoder block, benefiting the whole 3D detection to be better depth-guided. Also, we argue that the depth cross-attention layer should use the vanilla global attention instead of deformable attention, denoted as 'Deform. Depth CA', which hurts the performance due to its local receptive fields.

**Depth Positional Encodings**  $p_D$ . In Table 5, we explore different depth positional encodings for  $f_D^e$ in the depth cross-attention. By default, we apply the meter-wise encodings  $p_D \in \mathbb{R}^{(d_{max}-d_{min}+1)\times C}$ that assign one learnable embedding per meter and require depth interpolation for output. We then assign one learnable embedding for each depth bin, denoted as 'k-bin  $p_D \in \mathbb{R}^{k \times \bar{C}}$ ', and also experiment sinusoidal functions to encode either the depth values or 2D coordinates of the feature map, denoted as 'Depth sin/cos' and '2D sin/cos', respectively. As shown, 'meter-wise  $p_D$ ' performs the best for encoding more fine-grained depth cues ranging from  $d_{min}$  to  $d_{max}$ , which provides the queries with more scene-level spatial structures.

#### 5 Visualization

We visualize the attention maps  $A_D$  in Eq. 3 of the depth cross-attention at the third decoder block. As shown in Figure 4, the areas with high attention values spread over the entire image and also focus on some other objects. This indicates the query is able to adaptively capture long-range depth cues from others and the backgrounds, which is no longer limited by neighboring features.

## Conclusion

We propose MonoDETR, the first DETR-based framework for monocular 3D object detection, which contains minimal geometric priors and is free from any additional inputs, anchors or NMS. Different from existing center-guided methods, we enable object queries to explore depth cues adaptively from informative regions, and conducts inter-object and object-scene depth interactions. Extensive experiments and analyses have demonstrated the effectiveness of our approach. We hope MonoDETR could serve as a transformer baseline for future researches in monocular 3D object detection. Limitations. How to effectively incorporate the 3D geometric priors into our transformer framework is not discussed in the paper. Future work will focus on this direction to further improve the performance. Societal Impact. We do not foresee negative social impact from the proposed work.

#### A Details of the Loss Functions

After the depth-guided transformer, we adopt detection heads to estimate the attributes for each object query. All queries share the head weights for the same attribute. Specifically, we utilize one linear projection layer for the object category, three-layer MLP for 2D size (l, r, t, b) and projected 3D center  $(x_{3D}, y_{3D})$ , and two-layer MLP for depth  $d_{reg}$ , 3D size  $(h_{3D}, w_{3D}, l_{3D})$  and orientation  $\alpha$ .

**Object Category and 2D Size** (l, r, t, b). We detect objects of three categories in KITTI [14], car, pedestrian and cyclist, and adopt Focal loss [21] for optimization, denoted as  $\mathcal{L}_{class}$ . Referring to FCOS [38], we obtain the 2D bounding box of an object by predicting the distances from its four sides, l, r, t, b, to the projected 3D center  $(x_{3D}, y_{3D})$ . We apply L1 loss for the distances and GIoU loss [32] for the recovered 2D bounding box following DETR [5], denoted as  $\mathcal{L}_{lrtb}$  and  $\mathcal{L}_{GIoU}$ , respectively.

**Projected 3D Center**  $(x_{3D}, y_{3D})$ . We directly output the coordinate  $(x_{3D}, y_{3D})$  of each query's projected 3D center on the image, which thus discards two widely-adopted offsets. The first is the 2D-to-3D offset for recovering the projected 3D center from the predicted 2D center. The second is the quantization offset caused by the downsampled heatmap, which is a requisite for existing center-guided methods. By this, we can obtain the projected 3D center of each object in one step without the error of intermediate offsets, contributing to better localization accuracy. We adopt L1 loss for the center estimation and denote it as  $\mathcal{L}_{xy3D}$ .

**3D Size**  $(h_{3D}, w_{3D}, l_{3D})$  and Orientation  $\alpha$ . Instead of predicting the residuals to the mean shape values, we follow MonoDLE [26] to use the 3D IoU oriented loss for 3D sizes. We divide the heading angle into multiple bins with residuals and adopt MultiBin loss [9, 50] to optimize the prediction of orientation. The two losses are respectively denoted as  $\mathcal{L}_{size3D}$  and  $\mathcal{L}_{orien}$ .

**Depth**  $d_{pred}$ . As illustrated in Section 3.3 of the main paper, we average three depth values,  $d_{reg}$ ,  $d_{geo}$ , and  $d_{map}(x_{3D}, y_{3D})$ , to generate  $d_{pred}$ . We then adopt Laplacian aleatoric uncertainty loss [9] for the overall  $d_{pred}$ , formulated as

$$\mathcal{L}_{depth} = \frac{\sqrt{2}}{\sigma} \|d_{gt} - d_{pred}\|_1 + \log(\sigma), \tag{6}$$

where  $\sigma$  denotes the standard deviation predicted together with  $d_{reg}$ , and  $d_{gt}$  denotes the ground-truth depth label of the object.

**Two Groups of Losses**  $\mathcal{L}_{2D}$  **and**  $\mathcal{L}_{3D}$ . For bipartite matching, we calculate the matching cost of each query-label pair only by the group of  $\mathcal{L}_{2D}$ , formulated as

$$\mathcal{L}_{2D} = \lambda_1 \mathcal{L}_{class} + \lambda_2 \mathcal{L}_{xy3D} + \lambda_3 \mathcal{L}_{lrtb} + \lambda_4 \mathcal{L}_{GIoU}, \tag{7}$$

where we set  $\lambda_{1\sim 4}$  as 2, 10, 5, 2, respectively. For  $\mathcal{L}_{3D}$  in the final loss, we simply sum other 3D-related losses without weights as

$$\mathcal{L}_{3D} = \mathcal{L}_{size3D} + \mathcal{L}_{orien} + \mathcal{L}_{depth}. \tag{8}$$

# **B** Additional Results

Car Category on KITTI val Set. We list more results of the car category on KITTI val set under different IoU thresholds in Table 6, where our MonoDETR all achieves the highest detection accuracy. Compared to the second-best MonoDTR [17] that is a center-guided method with external depth supervision, our MonoDETR only requires object-wise depth labels and surpasses it by significant gains, e.g., +4.53%  $AP_{BEV}$ @IoU=0.7 and +4.83%  $AP_{3D}$ @IoU=0.5 for the easy level.

**Pedestrian and Cyclist Categories.** In Table 7, we report the scores for pedestrian and cyclist categories on KITTI *test* set both under the IoU threshold of 0.5. As these two categories contain much fewer training samples than car, it is more challenging for the network to accurately detect them. As shown, MonoDETR achieves superior  $AP_{3D}$  to other methods without additional data, indicating our generalization ability on other categories.

Table 6: **Performance of the car category on KITTI** *val* **sets under different IoU thresholds.** We utilize bold numbers to highlight the best results, and blue for the second-best ones.

Method	$AP_B$	$_{EV}$ @IoU	J=0.7	$AP_3$	<sub>3D</sub> @IoU:	=0.5	$AP_B$	$_{EV}$ @IoU	J=0.5
Method	Easy	Mod.	Hard	Easy	Mod.	Hard	Easy	Mod.	Hard
SMOKE [22]	19.99	15.61	15.28	_	-	-	-	-	-
MonoPair [9]	24.12	18.17	15.76	55.38	42.39	37.99	61.06	47.63	41.92
MonoRCNN [34]	25.29	19.22	15.30	-	-	-	-	-	-
MonoDLE [26]	24.97	19.33	17.01	55.41	43.42	37.81	60.73	46.87	41.89
IAFA [49]	22.75	19.60	19.21	-	-	-	-	-	-
MonoGeo [47]	27.15	21.17	18.35	56.59	43.70	39.37	61.96	47.84	43.10
RTM3D [19]	24.74	22.03	18.05	52.59	40.96	34.95	56.90	44.69	41.75
GUPNet [24]	31.07	22.94	19.75	57.62	42.33	37.59	61.78	47.06	40.88
MonoDTR [17]	33.33	25.35	21.68	64.03	47.32	42.20	69.04	52.47	45.90
MonoDETR (Ours)	37.86	26.95	22.80	68.86	48.92	43.57	72.30	53.10	46.62
Improvement	+4.53	+1.60	+1.12	+4.83	+1.60	+1.37	+3.26	+0.63	+0.72

Table 7: **Performance of the pedestrian and cyclist categories on KITTI** *test* **set.** We utilize bold numbers to highlight the best results, and blue ones for the second-best ones.

Method	Pede	estrian, A	$P_{3D}$	Cyclist, $AP_{3D}$			
Method	Easy	Mod.	Hard	Easy	Mod.	Hard	
Movi3D [35]	8.99	5.44	4.57	1.08	0.63	0.70	
MonoGeo [47]	8.00	5.63	4.71	4.73	2.93	2.58	
MonoFlex [46]	9.43	6.31	5.26	4.17	2.35	2.04	
MonoDLE [26]	9.64	6.55	5.44	4.59	2.66	2.45	
MonoPair [9]	10.02	6.68	5.53	3.79	2.12	1.83	
MonoDETR (Ours)	12.54	7.89	6.65	7.33	4.18	2.92	
Improvement	+2.52	+1.21	+1.12	+2.60	+1.25	+0.34	

# C Additional Ablation Study

**Depth Discretization.** We explore different depth discretization methods for the foreground depth map  $d_{fg}$  in Table 8. 'UD', 'SID' and 'LID' denote uniform, spacing-increasing, and linear-increasing discretizations, respectively. Instead of the weighted summation of depth bins, 'LID + argmax' outputs the depth value of the most confident bin. For 'Continuous Rep.', we directly regress the continuous depth value and optimize it by L1 loss. As reported, 'LID' performs the best than other discretization methods, since the linear-increasing intervals can suppress the larger estimation errors of farther objects. Also, 'LID' with weighted summation outperforms 'LID + argmax' for aggregating more depth cues from the predicted confidence of other depth bins.

**Bipartite Matching.** Our best solution only utilizes  $\mathcal{L}_{2D}$  as the matching cost for each query-label pair. We investigate how it performs to append more 3D losses into the matching cost. As reported in Table 9, adding  $\mathcal{L}_{size3D}$  or  $\mathcal{L}_{orien}$  would adversely influence the performance due to their unstable prediction during training. Further, adding  $\mathcal{L}_{depth}$  or the whole  $\mathcal{L}_{3D}$  even leads to training collapse, which is caused by the ill-posed depth estimation from monocular images.

**Transformer Blocks and FFN Channels.** In Table 10, we experiment different block numbers of the visual encoder and depth-guided decoder, along with the latent channels of FFN. As reported, MonoDETR achieves the best performance with 3-block visual encoder, 3-block depth-guided decoder, and 256-channel FFN. Different from DETR's [5] 6-block encoder, 6-block decoder, and 1024-channel FFN, MonoDETR adopts a lighter transformer architecture for the limited training samples in KITTI [14] dataset.

Table 8: The design of depth discretization in the foreground depth map. 'Continuous Rep.' denotes the continuous representation of depth.

Table 9:**The design of bipartite matching.** We set different losses as the matching cost of each query-label pair. '-' denotes training collapse.

Settings	Easy	Mod.	Hard
LID	28.84	20.61	16.38
UD	25.61	18.90	15.49
SID	26.05	18.95	15.59
LID + argmax	21.61	15.21	12.13
Continuous Rep.	24.36	17.24	14.48

Matching Cost	Easy	Mod.	Hard
$\mathcal{L}_{2D}$	28.84	20.61	16.38
w $\mathcal{L}_{size3D}$	27.13	19.21	15.93
w $\mathcal{L}_{orien}$	25.78	18.63	15.12
w $\mathcal{L}_{depth}$	-	-	-
w $\mathcal{L}_{3D}$	-	-	-

Table 10: Transformer blocks and FFN channels. FFN denotes the feed-forward neural network.

	Set.	Easy	Mod.	Hard
Visual	2	26.72	18.73	15.43
Encoder Blocks	3	28.84	20.61	16.38
Lileodel Blocks	4	27.37	20.04	16.09
Depth-guided	2	25.55	18.58	15.41
1 0	3	28.84	20.61	16.38
Decoder Blocks	4	25.31	18.29	15.11
	256	28.84	20.61	16.38
FFN Channels	512	27.24	18.93	15.54
	1024	26.77	19.07	15.87

# **D** Additional Implementation Details

For data augmentation on KITTI *test* set, we adopt random flip and photometric distortion following previous works [46, 26, 50], but for the *val* set, we also use random crop to further boost the performance. For training stability, we discard the training samples with depth labels larger than 65 meters or smaller than 2 meters. During inference, we simply filter out the object queries with the category confidence lower than 0.2 without NMS post-processing, and recover the 3D bounding box using the predicted six attributes following previous works.

# E Additional Visualization

In Figure 5, we show the detection results of our MonoDETR and the variant without the depth-guided transformer. Benefited from the depth guidance, MonoDETR obtains a global understanding of the scene-level spatial structure and the inter-object relations. This enables MonoDETR to well detect the objects occluded by others or truncated by images, and filter out the objects of ignored categories, e.g., van and truck.

# F Depth Error Analysis

To demonstrate the effectiveness of our depth-guided design, we show the depth error comparison for different variants of MonoDETR. We utilize four network variants illustrated in the first ablation study in Section 4.3 of the main paper, denoted as '(a), (b), (c), (d)' in Figure 6 and Table 11. We calculate their predicted mean depth errors and standard deviations on KITTI val set. With our depth-guided transformer, the depth estimation can be well benefited, which reduces the mean error from 1.54 meters to 1.35 meters and improves the  $AP_{3D}$  by +5.46% under the moderate level. In addition, our best solution of 20.61%  $AP_{3D}$  performs lower error variance of  $\pm 2.07$  than others, indicating our depth-guided transformer can produce more stable depth estimation of objects.



Figure 5: **Visualization of detection results.** We utilize green boxes for the variant without depth-guided transformer (Left) and yellow boxes for MonoDETR (Right). We use red circles to emphasize the detection difference.

Figure 6: **Depth errors for different variants of MonoDETR.** The x axis and y axis denote the  $AP_{3D}$  under the moderate level and the mean depth errors on KITTI val set, respectively.

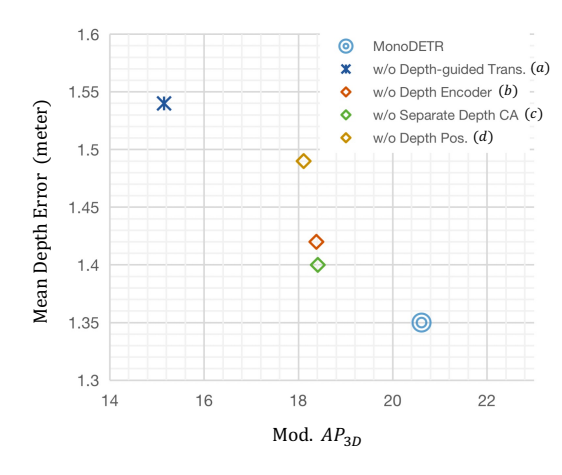


Table 11: Quantitative results of depth errors. We construct four network variants of MonoDETR by removing one of the components at a time. We respectively remove the depth-guided transformer, depth encoder, separate depth cross-attention layer, and depth positional encodings, denoted as '(a), (b), (c), (d)'. We show their  $AP_{3D}$  under the moderate level and the mean depth errors with standard deviations.

Architecture	$AP_{3D}\uparrow$	Depth Error ↓
MonoDETR	20.61	1.35±2.07
(a)	15.15	$1.54 \pm 2.29$
(b)	18.38	$1.42 \pm 2.10$
(c)	18.41	$1.40\pm 2.11$
(d)	18.11	$1.49 \pm 2.29$

#### References

- [1] Navaneeth Bodla, Bharat Singh, Rama Chellappa, and Larry S Davis. Soft-nms-improving object detection with one line of code. In *Proceedings of the IEEE international conference on computer vision*, pages 5561–5569, 2017. 3
- [2] Garrick Brazil and Xiaoming Liu. M3d-rpn: Monocular 3d region proposal network for object detection. In *IEEE International Conference on Computer Vision*, 2019. 1, 3
- [3] Garrick Brazil, Gerard Pons-Moll, Xiaoming Liu, and Bernt Schiele. Kinematic 3d object detection in monocular video. In *Proceedings of the European Conference on Computer Vision*, 2020. 7
- [4] Nicolas Carion, Francisco Massa, Gabriel Synnaeve, Nicolas Usunier, Alexander Kirillov, and Sergey Zagoruyko. End-to-end object detection with transformers. In *European conference on computer vision*, pages 213–229. Springer, 2020. 3
- [5] Nicolas Carion, Francisco Massa, Gabriel Synnaeve, Nicolas Usunier, Alexander Kirillov, and Sergey Zagoruyko. End-to-end object detection with transformers. In *Proceedings of the European Conference on Computer Vision*, 2020. 6, 7, 10, 11
- [6] Hansheng Chen, Yuyao Huang, Wei Tian, Zhong Gao, and Lu Xiong. Monorun: Monocular 3d object detection by reconstruction and uncertainty propagation. In *IEEE Conference on Computer Vision and Pattern Recognition (CVPR)*, 2021. 3, 7
- [7] Xiaozhi Chen, Kaustav Kundu, Ziyu Zhang, Huimin Ma, Sanja Fidler, and Raquel Urtasun. Monocular 3d object detection for autonomous driving. In *IEEE Conference on Computer Vision and Pattern Recognition*, 2016.
- [8] Xiaozhi Chen, Kaustav Kundu, Yukun Zhu, Andrew G. Berneshawi, Huimin Ma, Sanja Fidler, and Raquel Urtasun. 3d object proposals for accurate object class detection. In *Conference on Neural Information Processing Systems*, 2015. 1, 7
- [9] Yongjian Chen, Lei Tai, Kai Sun, and Mingyang Li. Monopair: Monocular 3d object detection using pairwise spatial relationships. In *IEEE Conference on Computer Vision and Pattern Recognition*, 2020. 3, 7, 10, 11
- [10] Zhigang Dai, Bolun Cai, Yugeng Lin, and Junying Chen. Up-detr: Unsupervised pre-training for object detection with transformers. In *Proceedings of the IEEE/CVF Conference on Computer Vision and Pattern Recognition*, pages 1601–1610, 2021. 3
- [11] Mingyu Ding, Yuqi Huo, Hongwei Yi, Zhe Wang, Jianping Shi, Zhiwu Lu, and Ping Luo. Learning depth-guided convolutions for monocular 3d object detection. In *IEEE Conference on Computer Vision and Pattern Recognition*, 2020. 3, 7
- [12] Peng Gao, Minghang Zheng, Xiaogang Wang, Jifeng Dai, and Hongsheng Li. Fast convergence of detr with spatially modulated co-attention. In *Proceedings of the IEEE/CVF International Conference on Computer Vision (ICCV)*, pages 3621–3630, October 2021. 3

- [13] Ravi Garg, Vijay Kumar BG, and Ian Reid. Unsupervised cnn for single view depth estimation: Geometry to the rescue. In *Proceedings of the European Conference on Computer Vision*, 2016.
- [14] Andreas Geiger, Philip Lenz, and Raquel Urtasun. Are we ready for autonomous driving? the kitti vision benchmark suite. In 2012 IEEE Conference on Computer Vision and Pattern Recognition, pages 3354–3361, 2012. 7, 10, 11
- [15] Clement Godard, Oisin Mac Aodha, and Gabriel J Brostow. Unsupervised monocular depth estimation with leftright consistency. In *IEEE Conference on Computer Vision and Pattern Recognition*, 2017. 1
- [16] Kaiming He, Xiangyu Zhang, Shaoqing Ren, and Jian Sun. Deep residual learning for image recognition. In *Proceedings of the IEEE Conference on Computer Vision and Pattern Recognition (CVPR)*, June 2016. 4, 7
- [17] Kuan-Chih Huang, Tsung-Han Wu, Hung-Ting Su, and Winston H Hsu. Monodtr: Monocular 3d object detection with depth-aware transformer. *arXiv preprint arXiv:2203.10981*, 2022. 3, 7, 10, 11
- [18] Alex H. Lang, Sourabh Vora, Holger Caesar, Lubing Zhou, Jiong Yang, and Oscar Beijbom. Pointpillars: Fast encoders for object detection from point clouds. In *IEEE Conference on Computer Vision and Pattern Recognition*, 2019. 1
- [19] Peixuan Li, Huaici Zhao, Pengfei Liu, and Feidao Cao. Rtm3d: Real-time monocular 3d detection from object keypoints for autonomous driving. In *European Conference on Computer Vision*, 2020. 3, 7, 11
- [20] Tsung-Yi Lin, Piotr Dollár, Ross Girshick, Kaiming He, Bharath Hariharan, and Serge Belongie. Feature pyramid networks for object detection. In *IEEE Conference on Computer Vision and Pattern Recognition*, 2017. 3
- [21] Tsung-Yi Lin, Priya Goyal, Ross Girshick, Kaiming He, and Piotr Dollár. Focal loss for dense object detection. In *IEEE Conference on Computer Vision and Pattern Recognition*, 2017. 1, 3, 5, 10
- [22] Zechen Liu, Zizhang Wu, and Roland Tóth. SMOKE: single-stage monocular 3d object detection via keypoint estimation. *CoRR*, abs/2002.10111, 2020. 3, 7, 11
- [23] Zongdai Liu, Dingfu Zhou, Feixiang Lu, Jin Fang, and Liangjun Zhang. Autoshape: Real-time shape-aware monocular 3d object detection. *CoRR*, abs/2108.11127, 2021. 3, 7
- [24] Yan Lu, Xinzhu Ma, Lei Yang, Tianzhu Zhang, Yating Liu, Qi Chu, Junjie Yan, and Wanli Ouyang. Geometry uncertainty projection network for monocular 3d object detection. In *Proceedings of the IEEE/CVF International Conference on Computer Vision (ICCV)*, pages 3111–3121, October 2021. 1, 2, 3, 7, 11
- [25] Xinzhu Ma, Shinan Liu, Zhiyi Xia, Hongwen Zhang, Xingyu Zeng, and Wanli Ouyang. Rethinking pseudo-lidar representation. In *Proceedings of the European Conference on Computer Vision (ECCV)*, 2020. 3, 7
- [26] Xinzhu Ma, Yinmin Zhang, Dan Xu, Dongzhan Zhou, Shuai Yi, Haojie Li, and Wanli Ouyang. Delving into localization errors for monocular 3d object detection. In *Proceedings of the IEEE/CVF Conference on Computer Vision and Pattern Recognition (CVPR)*, pages 4721–4730, June 2021. 1, 3, 7, 10, 11, 12
- [27] Depu Meng, Xiaokang Chen, Zejia Fan, Gang Zeng, Houqiang Li, Yuhui Yuan, Lei Sun, and Jingdong Wang. Conditional detr for fast training convergence. In *Proceedings of the IEEE/CVF International Conference on Computer Vision*, pages 3651–3660, 2021. 3
- [28] Ishan Misra, Rohit Girdhar, and Armand Joulin. An end-to-end transformer model for 3d object detection. In *Proceedings of the IEEE/CVF International Conference on Computer Vision*, pages 2906–2917, 2021. 3
- [29] Arsalan Mousavian, Dragomir Anguelov, John Flynn, and Jana Kosecka. 3d bounding box estimation using deep learning and geometry. In *IEEE Conference on Computer Vision and Pattern Recognition*, 2017. 3
- [30] Cody Reading, Ali Harakeh, Julia Chae, and Steven L. Waslander. Categorical depth distributionnetwork for monocular 3d object detection. *CVPR*, 2021. 3, 4, 7
- [31] Shaoqing Ren, Kaiming He, Ross Girshick, and Jian Sun. Faster r-cnn: Towards real-time object detection with region proposal networks. *Advances in neural information processing systems*, 28, 2015. 1, 3
- [32] Hamid Rezatofighi, Nathan Tsoi, JunYoung Gwak, Amir Sadeghian, Ian Reid, and Silvio Savarese. Generalized intersection over union: A metric and a loss for bounding box regression.

- In Proceedings of the IEEE/CVF conference on computer vision and pattern recognition, pages 658–666, 2019. 10
- [33] Shaoshuai Shi, Xiaogang Wang, and Hongsheng Li. Pointrcnn: 3d object proposal generation and detection from point cloud. In *IEEE Conference on Computer Vision and Pattern Recognition*, 2019. 1
- [34] Xuepeng Shi, Qi Ye, Xiaozhi Chen, Chuangrong Chen, Zhixiang Chen, and Tae-Kyun Kim. Geometry-based distance decomposition for monocular 3d object detection. In *IEEE International Conference on Computer Vision*, 2021. 7, 11
- [35] Andrea Simonelli, Samuel Rota Bulò, Lorenzo Porzi, Elisa Ricci, and Peter Kontschieder. Towards generalization across depth for monocular 3d object detection. In *Proceedings of the European Conference on Computer Vision*, 2020. 11
- [36] Peize Sun, Rufeng Zhang, Yi Jiang, Tao Kong, Chenfeng Xu, Wei Zhan, Masayoshi Tomizuka, Lei Li, Zehuan Yuan, Changhu Wang, et al. Sparse r-cnn: End-to-end object detection with learnable proposals. In *Proceedings of the IEEE/CVF Conference on Computer Vision and Pattern Recognition*, pages 14454–14463, 2021. 3
- [37] Zhiqing Sun, Shengcao Cao, Yiming Yang, and Kris M Kitani. Rethinking transformer-based set prediction for object detection. In *Proceedings of the IEEE/CVF International Conference on Computer Vision*, pages 3611–3620, 2021. 3
- [38] Zhi Tian, Chunhua Shen, Hao Chen, and Tong He. Fcos: Fully convolutional one-stage object detection. In *Proceedings of the IEEE/CVF international conference on computer vision*, pages 9627–9636, 2019. 1, 3, 10
- [39] Ashish Vaswani, Noam Shazeer, Niki Parmar, Jakob Uszkoreit, Llion Jones, Aidan N Gomez, Łukasz Kaiser, and Illia Polosukhin. Attention is all you need. *Advances in neural information processing systems*, 30, 2017. 3
- [40] Li Wang, Liang Du, Xiaoqing Ye, Yanwei Fu, Guodong Guo, Xiangyang Xue, Jianfeng Feng, and Li Zhang. Depth-conditioned dynamic message propagation for monocular 3d object detection. In *Proceedings of the IEEE/CVF Conference on Computer Vision and Pattern Recognition (CVPR)*, pages 454–463, June 2021. 3, 7
- [41] Tai Wang, Xinge Zhu, Jiangmiao Pang, and Dahua Lin. Fcos3d: Fully convolutional one-stage monocular 3d object detection. In *Proceedings of the IEEE/CVF International Conference on Computer Vision*, pages 913–922, 2021. 1, 3
- [42] Tai Wang, Xinge Zhu, Jiangmiao Pang, and Dahua Lin. Probabilistic and geometric depth: Detecting objects in perspective. In *Conference on Robot Learning*, 2021. 3, 7
- [43] Yue Wang, Vitor Campagnolo Guizilini, Tianyuan Zhang, Yilun Wang, Hang Zhao, and Justin Solomon. Detr3d: 3d object detection from multi-view images via 3d-to-2d queries. In *Conference on Robot Learning*, pages 180–191. PMLR, 2022. 3
- [44] Yingming Wang, Xiangyu Zhang, Tong Yang, and Jian Sun. Anchor detr: Query design for transformer-based detector. *arXiv preprint arXiv:2109.07107*, 2021. 3
- [45] Zhuyu Yao, Jiangbo Ai, Boxun Li, and Chi Zhang. Efficient detr: Improving end-to-end object detector with dense prior. *arXiv preprint arXiv:2104.01318*, 2021. 3
- [46] Yunpeng Zhang, Jiwen Lu, and Jie Zhou. Objects are different: Flexible monocular 3d object detection. In *Proceedings of the IEEE/CVF Conference on Computer Vision and Pattern Recognition (CVPR)*, pages 3289–3298, June 2021. 1, 2, 3, 7, 11, 12
- [47] Yinmin Zhang, Xinzhu Ma, Shuai Yi, Jun Hou, Zhihui Wang, Wanli Ouyang, and Dan Xu. Learning geometry-guided depth via projective modeling for monocular 3d object detection. *arXiv preprint arXiv:2107.13931*, 2021. 1, 2, 7, 11
- [48] Minghang Zheng, Peng Gao, Xiaogang Wang, Hongsheng Li, and Hao Dong. End-to-end object detection with adaptive clustering transformer. *arXiv preprint arXiv:2011.09315*, 2020. 3
- [49] Dingfu Zhou, Xibin Song, Yuchao Dai, Junbo Yin, Feixiang Lu, Miao Liao, Jin Fang, and Liangjun Zhang. Iafa: Instance-aware feature aggregation for 3d object detection from a single image. In *Proceedings of the Asian Conference on Computer Vision*, 2020. 7, 11
- [50] Xingyi Zhou, Dequan Wang, and Philipp Krähenbühl. Objects as points. *CoRR*, abs/1904.07850, 2019. 1, 3, 10, 12
- [51] Yin Zhou and Oncel Tuzel. Voxelnet: End-to-end learning for point cloud based 3d object detection. In *IEEE Conference on Computer Vision and Pattern Recognition*, 2018. 1
- [52] Xizhou Zhu, Weijie Su, Lewei Lu, Bin Li, Xiaogang Wang, and Jifeng Dai. Deformable detr: Deformable transformers for end-to-end object detection. *arXiv preprint arXiv:2010.04159*, 2020. 3, 7, 9